Chem. Mater. **2002,** *14,* 1091−1097

Dependence of Ionic Conductivity on Composition of Fast Ionic Conductors $Li_{1+x}Ti_{2-x}Al_x(PO_4)_3$, $0 \leq x \leq 0.7$. A Parallel NMR and Electric Impedance Study

K. Arbi,* S. Mandal, J. M. Rojo, and J. Sanz

Instituto de Ciencia de Materiales de Madrid (ICMM), Consejo Superior de Investigaciones Científicas, Cantoblanco, 28049 Madrid, Spain

Received May 29, 2001. Revised Manuscript Received December 4, 2001

Materials with nominal compositions $Li_{1+x}Ti_{2-x}Al_x(PO_4)_3$, $0 \leq x \leq 0.7$, have been prepared and studied with X-ray diffraction (XRD), nuclear magnetic resonance (NMR), and electrical impedance techniques. Substitution of Ti^{4+} by Al^{3+} reduces the unit cell dimensions of the NASICON framework but enhances the grain interior conductivity. The overall conductivity is dominated by the grain boundary composition. Detection of new broad peaks in the ^{31}P and ^{27}Al MAS NMR spectra supports the formation of an amorphous Li-conducting phase that accounts for the increase observed in the overall conductivity. In samples with $x > 0.5$, crystallization of $Li_4P_2O_7$ as a segregated phase is accompanied by the appearance of a new electrical response. In these samples, a decrease in overall conductivity, associated with a modification of the amorphous phase, is also observed.

I. Introduction

Lithium-ion-conducting solids are materials of increasing interest because of their possible use as solid electrolytes in high-energy solid-state batteries. Compounds with the NASICON (Na superionic conductor) structure[1] and the formula $LiM^{IV}{}_2(PO_4)_3$, with M = Ge, Ti, Sn, Zr, and Hf, have been extensively studied[2−6] because of their good ionic conductivity. The NASICON framework is built up of $M_2(PO_4)_3$ units in which two MO_6 octahedra are linked to three PO_4 tetrahedra by shared oxygens. The usual symmetry is rhombohedral, space group $R\bar{3}c$, although in compositions with M = Sn, Zr, Hf, a triclinic phase has been reported.[7−9] In the rhombohedral phase, there are two different sites for alkali cations: (1) M_1 sites surrounded by six oxygen atoms and located at inversion centers and (2) M_2 sites surrounded by 10 oxygen and disposed symmetrically around ternary axes. Both sites are arranged in an alternating way along conducting channels. In rhombohedral $LiGe_2(PO_4)_3$ and $LiTi_2(PO_4)_3$ compounds, a preferential occupancy of the M1 sites has been deduced from neutron diffraction (ND) experiments.[10,11]

During the past few years, particular attention has been paid to titanium-based materials with the NASICON structure $Li_{1+x}Ti_{2-x}N_x(PO_4)_3$, $LiTi_{2-x}M_x(PO_4)_3$, and $Li_{1-x}Ti_{2-x}R_x(PO_4)_3$, where N, M, and R stand for tri-, tetra-, and pentavalent cations, respectively.[12−20] Aono et al.[12] showed that the conductivity was greatly enhanced upon substitution of Ti^{4+} by N^{3+} cations such as Al, Ga, Cr, In, Sc, Fe, and Y. The maximum conductivity obtained at 298 K was 7×10^{-4} S cm^{-1} in $Li_{1.3}M_{0.3}Ti_{1.7}$ $(PO_4)_3$, where M is Al or Sc. The same authors showed that an addition of Li_2O or $Li_4P_2O_7$ as a binder increased the density of the pellets and improved the overall conductivity of the samples considerably.[12,21] In recent studies on $Li_{1+x}Ti_{2-x}Al_x(PO_4)_3$ compounds, Wong et al.[13] identified the formation of a minor $AlPO_4$ phase that enhanced the sintering of pellets. However, the factors responsible for the improvement of the intrinsic and overall conductivities of

---

* To whom correspondence should be addressed.

(1) Goodenough, J. B.; Hong, H. Y−P.; Kafalas, J. A. *Mater. Res. Bull.* **1976**, *11*, 203−220.

(2) Winand, J. M.; Rulmont, A.; Tarte, P. *J. Solid State Chem.* **1991**, *93*, 341−349.

(3) Martinez-Juárez, A.; Rojo, J. M.; Iglesias, J. E.; Sanz, J. *Chem. Mater.* **1995**, *7* (10), 1857−1862.

(4) Sudreau, F.; Petit, D.; Boilot, J. P. *J. Solid State Chem.* **1989**, *83*, 78−90.

(5) París, M. A.; Martínez-Juárez, A.; Iglesias, J. E.; Rojo, J. M.; Sanz, J. *Chem. Mater.* **1997**, *9*, 1430−1436.

(6) Martinez-Juárez, A.; Pecharromán, C.; Iglesias, J. E.; Rojo, J. M. *J. Phys. Chem. B* **1998**, *102*, 372−375.

(7) Morin, E.; Angenault, J.; Couturier, J. C.; Quarton, M.; He, H.; Klinowski, J. *Eur. J. Solid State Inorg. Chem.* **1997**, *34*, 947−958.

(8) Catti, M.; Stramare, S.; Ibberson, R. *Solid State Ionics* **1999**, *123*, 173−180.

(9) Losilla, E. R.; Aranda, M. A. G.; Martinez-Lara, M.; Bruque, S. *Chem. Mater.* **1997**, *9*, 1678−1685.

(10) Alami, M.; Brochu, R.; Soubeyroux, J. L.; Graverau, P.; le Flem, G.; Hagenmuller, P. *J. Solid State Chem.* **1991**, *90*, 185−193.

(11) Tran Qui, D.; Hamdoune, S.; Soubeyroux, J. L.; Prince, E. *J. Solid State Chem.* **1988**, *72*, 309−315.

(12) Aono, H.; Sugimoto, E.; Sadaoka, Y.; Imanaka, N.; Adachi, G−Y. *J. Electrochem. Soc.* **1990**, *137*, 1023−1027.

(13) Wong, S.; Newman, P. J.; Best, A. S.; Nairn, K. M.; MacFarlane, D. R.; Forsyth, M. *J. Mater. Chem.* **1998**, *8*, 2199−2203.

(14) Subramanian, M. A.; Subramanian, R.; Clearfield, A. *Solid State Ionics* **1986**, *18−19*, 562−569.

(15) Chun, L. S.; Xiang, L. Z. *Solid State Ionics* **1983**, *9−10*, 835−838.

(16) Xiang, L. Z.; Jun, Y. H.; Chun, L. S.; Bao, T. S. *Solid State Ionics* **1986**, *18−19*, 549−552.

(17) Chun, L. S.; Yi, C. J.; Xiang, L. Z. *Solid State Ionics* **1988**, *28−30*, 1265−1270.

(18) Casciola, M.; Costantino, U.; Krogh Andersen, I. G.; Krogh Andersen, E. *Solid State Ionics* **1990**, *37*, 281−287.

(19) Taylor, B. E.; English, A. D.; Berzins, T. *Mater. Res. Bull.* **1977**, *12*, 171−182.

(20) Chowdari, B. V. R.; Radhakrishan, K.; Thomas, K. A.; Subba Rao, G. V. *Mater. Res. Bull.* **1989**, *24*, 221−229.

(21) Aono, H.; Sugimoto, E.; Sadaoka, Y.; Imanaka, N.; Adachi, G.-Y. *Solid State Ionics* **1991**, *47*, 257−264.

10.1021/cm010528i CCC: $22.00

the $\mathrm{Li}_{1+x}\mathrm{Ti}_{2-x}\mathrm{Al}_x(\mathrm{PO}_4)_3$ series are not yet well understood.

In this work, $\mathrm{Li}_{1+x}\mathrm{Ti}_{2-x}\mathrm{Al}_x(\mathrm{PO}_4)_3$ samples in the compositional range $0 \leq x \leq 0.7$ have been prepared and studied by XRD, NMR, and electric impedance techniques. The true composition of the materials is discussed, and the presence of secondary phases is analyzed. The information obtained on pellet composition has been correlated with the ionic conductivity. For that purpose, the grain interior and overall conductivities along the mentioned series were measured.

II. Experimental Section

Samples were prepared by heating at 950 °C stoichiometric mixtures of $\mathrm{Li_2CO_3}$ (≥99%), $\mathrm{TiO_2}$ (99%), $\mathrm{Al_2O_3}$ (99.99%), and $\mathrm{(NH_4)_2HPO_4}$ (≥99%). The reagents were first dried at 120 °C for 10 h and then mixed and heat treated in a platinum crucible at 180, 300, 500, 700, 800, 900, and 950 °C. After each treatment, the mixtures were ground in an agate mortar and analyzed by X-ray diffraction. The samples were stored for later use when the characteristic X-ray peaks of the reagents and/or intermediate compounds such as pyrophosphates were not detected.

X-ray diffraction patterns were recorded at room temperature with Cu Kα radiation in a PW-1710 Phillips diffractometer. Data were taken in the $10° \leq 2\theta \leq 70°$ range with 0.02° per step and a count of 0.5 s at each step. A small amount of Si (NIST, $a = 5.439\,040$ Å) was mixed with the sample in a second run to determine the correction to be applied to the peak positions. Lattice parameters were deduced by fitting the XRD patterns with the TREOR program.

Two-probe impedance measurements were carried out in a 1260 Solartron impedance/gain phase analyzer. The frequency range used was $5-10^7$ Hz. The measurements were made on sintered cylindrical pellets, obtained by cold pressing the powder samples and sintering them at 1000 °C for 24 h. Platinum was used as the electrode. The conductivity of the samples was measured in the temperature range 150−300 K in an Oxford cryostat. All measurements were done with the pellets under a dried nitrogen atmosphere.

^{7}Li, ^{27}Al, and ^{31}P MAS NMR spectra were obtained at room temperature in an MSL-400 Bruker spectrometer. The frequencies used for ^{7}Li, ^{27}Al and ^{31}P were 155.50, 104.26, and 161.97 MHz, respectively. Samples were spun at 4 and 10 kHz, and spectra were recorded after $\pi/2$ pulse irradiation (~4 μs). The recycle time between successive scans was 10 s for lithium and 5 s for aluminum and phosphorus. The number of scans was in the range of 40−800. The ^{7}Li, ^{27}Al, and ^{31}P chemical shift values are given relative to 1 M LiCl, 1 M $\mathrm{AlCl_3}$, and 85% $\mathrm{H_3PO_4}$ aqueous solutions. The fitting of the NMR spectra was carried out with the Bruker WINFIT program.[22] For quantitative purposes, the sum of the integrated intensities of the spinning sidebands corresponding to each component was determined.

III. Results

1. X-ray Powder Diffraction. XRD patterns of $\mathrm{Li}_{1+x}\mathrm{Ti}_{2-x}\mathrm{Al}_x(\mathrm{PO}_4)_3$ samples in the range $0 \leq x \leq 0.7$ are given in Figure 1a. The more intense reflections, which correspond to a rhombohedral symmetry ($R\bar{3}c$ space group), are ascribed to the NASICON-type compounds. For increasing Al contents, the XRD reflections shift toward higher 2θ positions, indicating a decrease in the unit cell dimensions. The a and c parameters of the corresponding hexagonal cell decrease as the Al content increases; however, for $x \leq 0.3$, the variation of the c parameter is more important than that of the a parameter (Figure 1b). For $x > 0.3$, the variation of both parameters becomes less important.

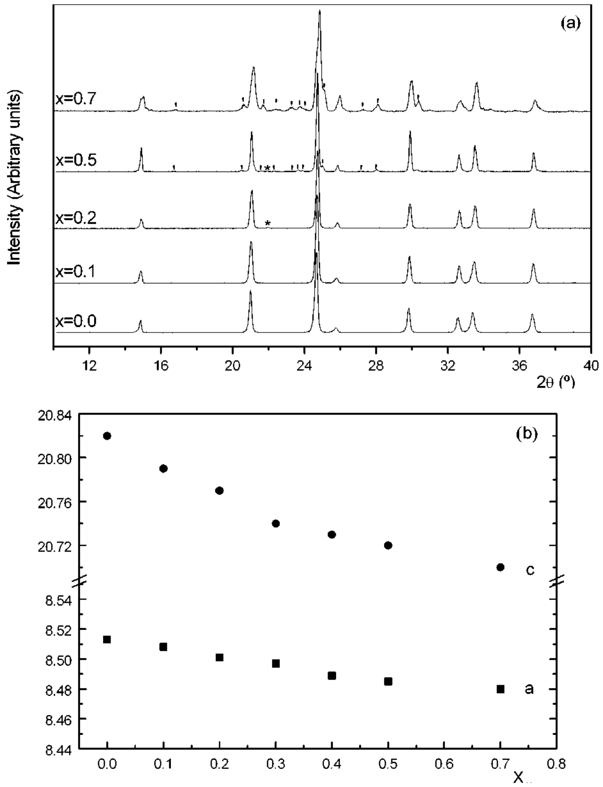

Figure 1. (a) X-ray powder diffraction patterns of $\mathrm{Li}_{1+x}\mathrm{Ti}_{2-x}\mathrm{Al}_x(\mathrm{PO}_4)_3$ samples. The small peak marked by the asterisk (*) corresponds to $\mathrm{AlPO_4}$, and the peaks marked by primes (′) correspond to $\mathrm{Li_4P_2O_7}$. (b) Hexagonal a and c parameters of the NASICON phase vs Al content.

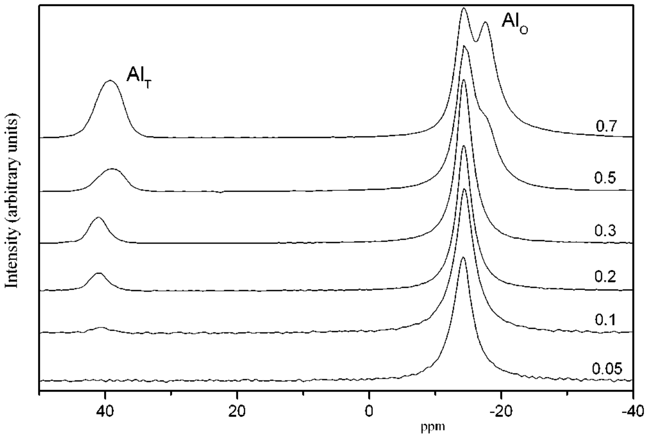

Figure 2. ^{27}Al MAS NMR spectra of the $\mathrm{Li}_{1+x}\mathrm{Ti}_{2-x}\mathrm{Al}_x(\mathrm{PO}_4)_3$ series. $\mathrm{Al_T}$ and $\mathrm{Al_O}$ represent tetrahedrally and octahedrally coordinated aluminum, respectively.

For $x \geq 0.2$, a small XRD reflection is observed at $2\theta = 22°$ (asterisks in Figure 1a). For $x \geq 0.5$, other new reflections are detected in the X-ray patterns (marks in Figure 1a) that indicate the formation of new crystalline phases. The intensities of these reflections increase as the Al content increases.

2. NMR Spectroscopy. *^{27}Al MAS NMR Spectroscopy.* ^{27}Al ($I = {}^5/_2$) MAS NMR spectra are formed by lines corresponding to the five possible nuclear transitions, modulated by equally spaced spinning sidebands as-

---

[22] Massiot, D. *WINFIT*; Bruker-Franzen Analytik GmbH: Bremen, Germany, 1993.

Table 1. Quadrupole Constant, C_Q (kHz), and Asymmetry Parameter, η, as Deduced from ^{7}Li MAS NMR Spectra. Chemical Shift δ_{iso} (ppm) Values Deduced from ^{7}Li, ^{27}Al, and ^{31}P MAS NMR Spectra of $Li_{1+x}Ti_{2-x}Al_x(PO_4)_3$ Samples

x_{Al}	x_{Al}^{NMR}	C_Q	η	Li	Al_O	Al_T	$P(Ti_4Al_0)$	$P(Ti_3Al_1)$	$P(Ti_2Al_2)$	$P(Ti_1Al_3)$	$P(Ti_0Al_4)$
0	0	44.2	0	−1.23	–	–	−27.56	–	–	–	–
0.05	0.044	43.1	0	−1.19	−14.28	–	−27.58	−26.42	−25.84	–	–
0.1	0.091	44.0	0	−1.22	−14.34	40.45	−27.57	−26.33	−25.43	–	–
0.2	0.21	44.1	0	−1.21	−14.28	40.98	−27.55	−26.02	−24.87	−23.32	–
0.3	0.34	44.2	0	−1.12	−14.28	40.98	−27.25	−25.95	−24.72	−23.25	–
0.5	0.46	46.1	0	−0.71	−14.37	38.90	−27.34	−26.05	−24.76	−23.39	–
0.7	0.52	47.8	0	0/−1	−14.28	39.34	−27.2	−25.8	−24.4	−22.95	−21.28

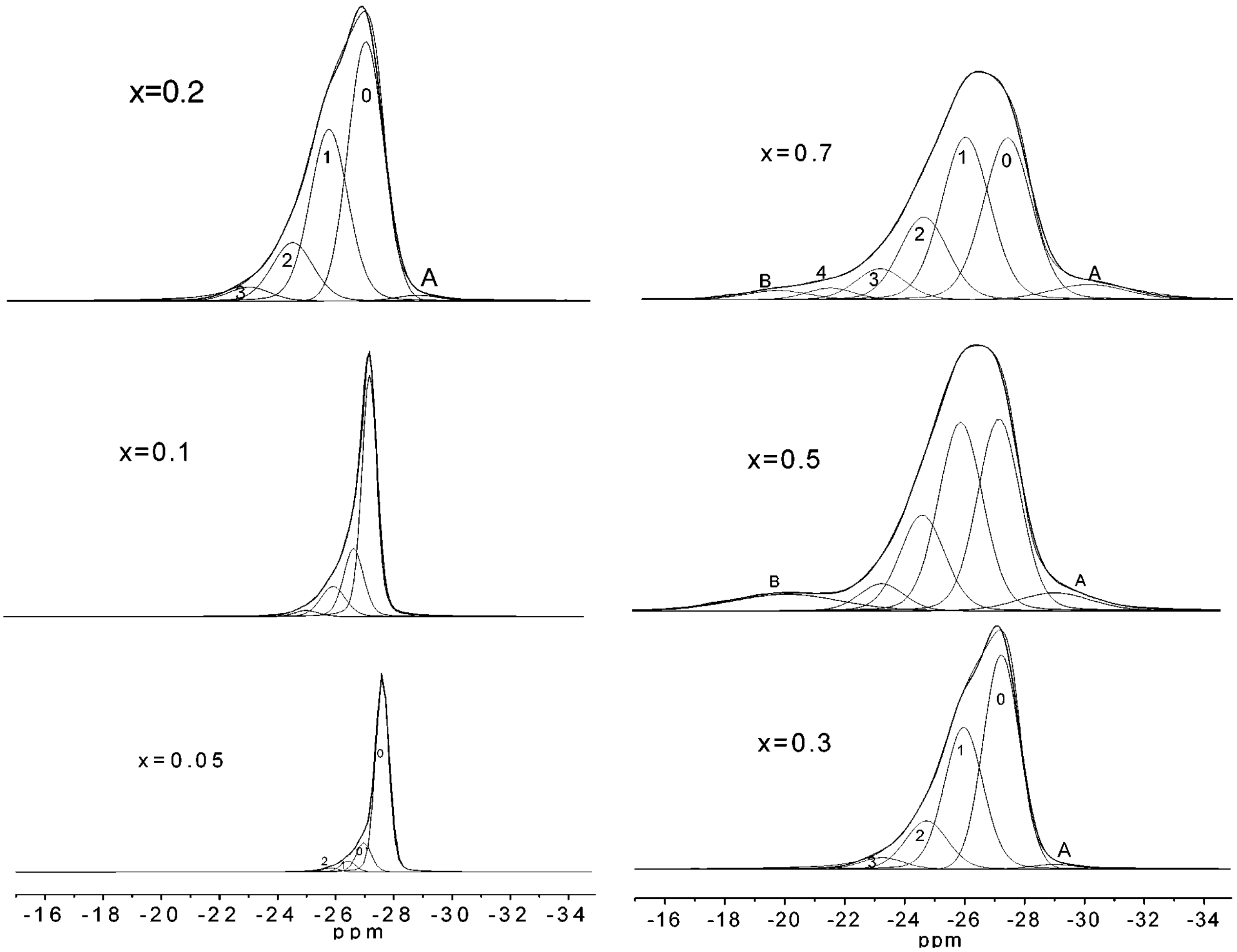

Figure 3. ^{31}P MAS NMR spectra of the $Li_{1+x}Ti_{2-x}Al_x(PO_4)_3$ series. The environments $P(OTi)_4$, $P(OTi)_3(OAl)_1$, $P(OTi)_2(OAl)_2$, $P(OTi)_1(OAl)_3$, and $P(OAl)_4$ are denoted by 0, 1, 2, 3, and 4, respectively (see text). Peaks corresponding to aluminum phosphate and lithium phosphate are denoted by A and B, respectively.

sociated with the rotation of the sample (not shown). The central line of the spectra is formed by two components (Figure 2). The more intense component at $\delta \approx -15$ ppm corresponds to aluminum in octahedral coordination (Al_O). The component at $\delta \approx 40$ ppm is ascribed to aluminum in tetrahedral coordination (Al_T). The positions of the two components along the series are given in Table 1.

As the Al content increases, the intensity of the Al_T band increases, and its position shifts slightly toward more positive values. However, in samples with $x_{Al} = 0.5$ and 0.7, this component shifts in the opposite sense and becomes broader. At the same time, another Al_O component is detected at −17 ppm, indicating the formation of new phases.

^{31}P MAS NMR Spectroscopy. ^{31}P ($I = {}^1/_2$) MAS NMR spectra of the analyzed samples are shown in Figure 3. For $x = 0$, a single line at −27.5 ppm is observed. For higher x, the line shifts toward more positive values and becomes asymmetrically broadened. This indicates the presence of other components.

In Figure 3, a deconvolution of the ^{31}P NMR spectra is given. For each sample, the line width and the separation between adjacent components were assumed to be constant. To describe the asymmetry of the main component of the samples with $x < 0.2$, two bands were used (peaks labeled 0 and 0′). In agreement with previous works,[23] the shift produced by substitution of Ti by Al was assumed to be additive, allowing for the identification of components associated with the $P(OTi)_4$, $P(OTi)_3(OAl)_1$, $P(OTi)_2(OAl)_2$, $P(OTi)_1(OAl)_3$, and $P(OAl)_4$ environments (bands labeled by the numbers 0, 1, 2, 3, and 4, respectively, in Figure 3). We observe that the

---

(23) Losilla, E. R.; Aranda, M. A. G.; Bruque, S.; París, M. A.; Sanz, J.; Campo, J.; West, A. R. *Chem. Mater.* **2000**, *12*, 2134−2142.

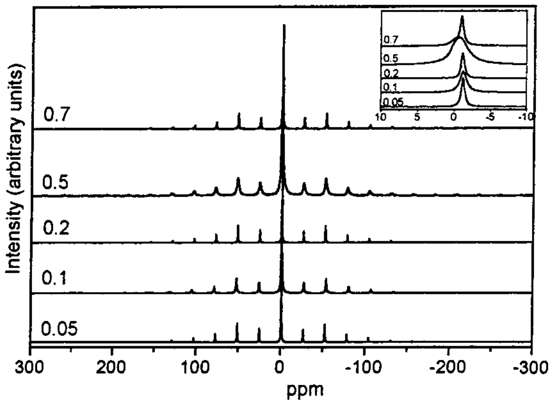

Figure 4. ^{7}Li MAS NMR spectra of the $Li_{1+x}Ti_{2-x}Al_x(PO_4)_3$ series. Equally spaced bands are produced by the rotation of the sample. The central lines of spectra are shown in detail in the inset.

intensity of the components located at less negative values becomes more intense as the aluminum content increases.

In the spectra of the samples with $x \geq 0.2$, another component of low intensity at approximately −29 ppm (line A) is detected; the intensity of this line increases as the Al content increases. In the spectra for $x = 0.5$ and 0.7, a new broad component at −20 ppm is also detected (line B). The positions of the components obtained after deconvolution of the spectra are given in Table 1.

^{7}Li MAS NMR Spectroscopy. ^{7}Li ($I = {}^3/_2$) MAS NMR spectra of the samples are shown in Figure 4. The spectra are formed by a central line ($-^1/_2$, $^1/_2$ transition) and two satellite lines ($-^3/_2$, $-^1/_2$ and $^1/_2$, $^3/_2$ transitions). Central and satellite lines are modulated by equally spaced spinning sidebands, the powder patterns of samples being reproduced by connecting the tops of the sidebands.

The full-width at half-maximum of the central transition is near 450 Hz in the static ^{7}Li NMR spectra (not shown). This parameter is considerably reduced when Li−P and Li−Li dipolar interactions are eliminated in MAS NMR experiments. In the inset of Figure 4, the central component of the ^{7}Li MAS NMR spectra of the series is shown. The line width of this component is almost constant for $x \leq 0.2$ but increases for $x > 0.2$. At the same time, a progressive shift of this component from −1.20 to −0.71 ppm is observed (Table 1). The increase in the line width is indicative of the presence of other environments for Li. In the case of $x = 0.7$, two components at −1 and 0 ppm are resolved.

Spinning sideband patterns were used to determine the quadrupole constant (C_Q) and the asymmetry parameter (η), both of which characterize the structural sites occupied by Li (see Table 1). Above $x = 0.3$, the number of spinning sidebands increases, indicating the presence of another phase. In samples with $x = 0.3$, 0.5, and 0.7, the ^{7}Li MAS NMR spectra are formed by two components, with quadrupole constants $C_Q^{(1)} = 40$ kHz and $C_Q^{(2)} = 110$ kHz. Finally, an increase of the $C_Q^{(1)}$ parameter of NASICON compounds is observed along the series (Table 1).

3. Impedance Measurements. The angular frequency dependence of the conductivity for the $x = 0.2$ sample is shown in Figure 5a. At 280 K, three regimes are observed: (i) an ill-defined dispersive regime below 10^2 s^{-1}; (ii) a plateau in the frequency range 10^2−10^4 s^{-1}, followed by a dispersive regime at around 10^6 s^{-1}; and (iii) an ill-defined plateau at about 10^7 s^{-1}, followed again by a dispersive regime. These three features correspond to the spike and the low- and high-frequency arcs observed in the impedance plots (not shown). At lower temperatures, 150 and 210 K, the three features are shifted toward lower frequencies. The experimental data were fitted with the expression

$$\sigma^* = 1/(1/\sigma_1^* + 1/\sigma_2^*)$$

where the first asterisk stands for the overall complex conductivity and σ_1* and σ_2* account for grain interior

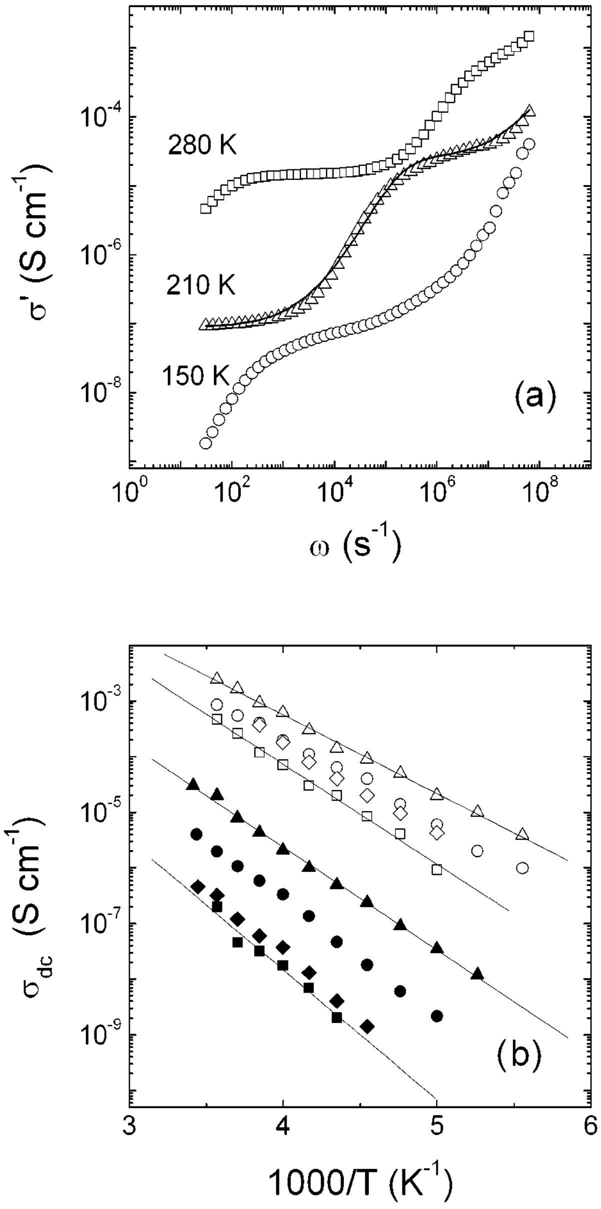

Figure 5. (a) Real conductivity vs angular frequency at indicated temperatures for the $x = 0.2$ sample. The solid line corresponds to the best fit of the data obtained at 210 K. (b) Grain interior (open symbols) and overall (closed symbols) dc conductivities vs reciprocal temperature (1000/*T*). Squares, diamonds, circles, and triangles represent samples with $x = 0$, 0.05, 0.1, and 0.2, respectively. The solid straight lines show the fittings to the Arrhenius equation.

Table 2. Activation Energy (E), Preexponential Factor (σ_0), and Conductivity Values (σ) at 298 K

	grain interior			new response			overall		
x_{Al}	E (eV)	σ_0 (S cm^{-1})	σ (S cm^{-1})	E (eV)	σ_0 (S cm^{-1})	σ (S cm^{-1})	E (eV)	σ_0 (S cm^{-1})	σ (S cm^{-1})
0	0.35 ± 0.01	1297 ± 651	1.6×10^{-3}	–	–	–	0.46 ± 0.04	102 ± 97	1.6×10^{-6}
0.05	0.33 ± 0.01	880 ± 379	2.3×10^{-3}	–	–	–	0.50 ± 0.02	394 ± 236	1.4×10^{-6}
0.1	0.30 ± 0.01	257 ± 58	2.2×10^{-3}	–	–	–	0.42 ± 0.02	64 ± 14	5.0×10^{-6}
0.2	0.28 ± 0.01	275 ± 56	5.1×10^{-3}	–	–	–	0.36 ± 0.01	64 ± 14	5.2×10^{-5}
0.5	0.28 ± 0.01	205 ± 64	3.8×10^{-3}	0.30 ± 0.01	17 ± 6	1.4×10^{-4}	0.35 ± 0.01	9 ± 3	1.1×10^{-5}
0.7	0.27 ± 0.01	109 ± 72	3.0×10^{-3}	0.30 ± 0.01	5 ± 2	4.2×10^{-5}	0.37 ± 0.01	16 ± 2	8.8×10^{-6}

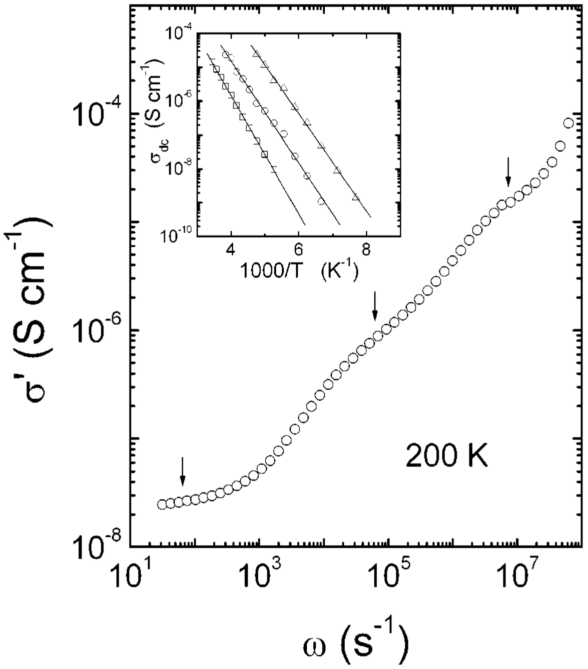

Figure 6. Real conductivity vs angular frequency for the $x = 0.5$ sample at 200 K. dc conductivities are measured at the points indicated by arrows (see text). Arrhenius plots of the three measured conductivities are shown in the inset.

and grain boundary contributions, respectively. To reproduce the overall conductivity, $\sigma_1{}^*$ and $\sigma_2{}^*$ were assumed to adopt the form[24] $\sigma_{dc} + B(i\omega)^n$. As an example, the fitting obtained at 210 K is shown as a solid line in Figure 5a. In this way, we separately estimated the dc conductivities for the grain interior and for the grain boundary, the latter being almost coincident with the overall dc conductivity of the pellet.

Variations of the grain interior and overall dc conductivity vs reciprocal temperature (1000/T) are shown for samples with $x \leq 0.2$ in Figure 5b. The experimental data are fitted to the Arrhenius expression

$$\sigma_{dc} = \sigma_0 \exp(-E/kT)$$

where σ_0 is a preexponential factor, E is the activation energy, k is the Boltzmann constant, and T is the temperature. Values of σ_0 and E deduced from the fittings are reported in Table 2.

The frequency dependence of the conductivity for the $x = 0.5$ sample, measured at 200 K, is shown in Figure 6. This plot is similar to that obtained for the $x = 0.7$ sample. We observe three plateaus marked by arrows: a well-defined plateau at low frequency and two ill-defined plateaus at higher frequencies. The dc conductivity is estimated by measuring the conductivity at the positions of the arrows. The conductivities deduced from the low-frequency (below 10^2 s^{-1}) and high-frequency (about 10^7 s^{-1}) plateaus are close to the overall and grain interior conductivities found for $x = 0.2$ sample at the same temperature. The conductivity deduced from the arrow at the middle-frequency plateau corresponds to a new response, which is characteristic of samples with high Al contents. Arrhenius plots corresponding to the three mentioned plateaus are shown (solid lines) in the inset of Figure 6. σ_0 and E values deduced from the fittings are listed in Table 2.

IV. Discussion

From the analysis of the overall conductivity of the $Li_{1+x}Ti_{2-x}Al_x(PO_4)_3$ series vs the Al content, a maximum in conductivity at $x = 0.2$ is observed (Table 2). Other authors have also reported this maximum; however, the causes responsible for this behavior are not well-known.[12,25] To understand the two regimes associated with the maximum, samples having different Al contents were studied by XRD and NMR techniques.

Samples with $x \leq 0.2$. The X-ray diffraction patterns of these samples were indexed by using the hexagonal unit cell of the NASICON-type compounds (hexagonal setting of the $R\bar{3}c$ space group). The progressive substitution of Ti^{4+} by Al^{3+} reduces the parameters of the hexagonal cell (Figure 1), in agreement with the smaller size of Al^{3+} (0.54 Å) compared to Ti^{4+} (0.60 Å).[26] This substitution is confirmed by the presence of octahedrally coordinated aluminum (Al_O) in the ^{27}Al NMR spectra. Thus, the NMR spectra show the line at approximately −15 ppm that is ascribed to Al located at the octahedral sites, which are occupied only by Ti^{4+} in the undoped $LiTi_2(PO_4)_3$ member.[13] Taking into account that each PO_4 tetrahedron in the NASICON framework shares its oxygens with four MO_6 (M = Ti, Al) octahedron, the identified ^{31}P NMR components were ascribed to the environments 4Ti, 3Ti1Al, 2Ti2Al, 1Ti3Al, and 4Al. The quantitative analysis of the NMR spectra allowed for an estimation of the Al content in the NASICON phases. The Al/Ti ratio was calculated according to the expression[23]

$$\frac{Al^{3+}}{Ti^{4+}} = \frac{4I_4 + 3I_3 + 2I_2 + I_1}{I_3 + 2I_2 + 3I_1 + 4I_0} = \frac{x}{2 - x}$$

where I_n (n = 0, 1, 2, 3, 4) represents the intensity of the bands associated with $(4 - n)$Ti(n)Al environments (Table 1). From the Al/Ti ratios, the octahedral Al content, x, was deduced and compared with the nominal

---

[24] Jonscher, A. K. In *Dielectric Relaxation in Solids*; Chelsea Dielectric Press: London, 1983.

[25] Forsyth, M.; Wong, S.; Nairn, K. M.; Best, A. S.; Newman, P. J.; MacFarlane, D. R. *Solid State Ionics* **1999**, *124*, 213−219.

[26] Shannon, R. D. *Acta Crystallogr.* **1976**, *A32*, 757−767.

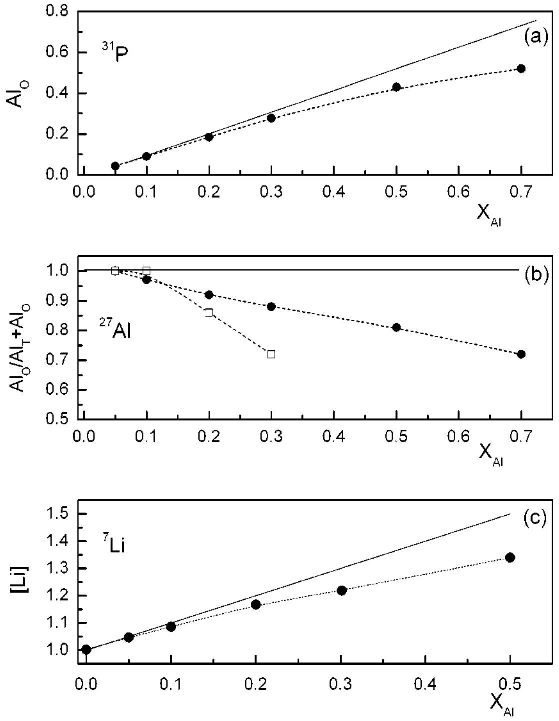

Figure 7. Plots of the octahedral Al content vs nominal Al content as deduced from (a) ^{31}P and (b) ^{27}Al NMR spectra. Open squares correspond to values reported in ref 13. (c) Plot of Li content vs nominal Al content as deduced from ^7Li MAS NMR spectra. The solid lines are the predicted Al_O and Li contents for the nominal $Li_{1+x}Ti_{2-x}Al_x(PO_4)_3$ compositions.

content (Figure 7a). It can be observed that, for $x \leq 0.2$, aluminum is mainly incorporated, as octahedral Al_O, into the NASICON framework. However, for $x > 0.2$, the experimental data are lower than expected (solid line), indicating that a significant part of Al must be placed outside of the NASICON phase. The presence of tetrahedral aluminum (Al_T), as indicated in the ^{27}Al MAS NMR spectra, is responsible for the decrease observed in the $Al_O/(Al_T + Al_O)$ ratio vs the Al content in Figure 7b. This finding was previously ascribed to the segregation of the $AlPO_4$ phase; however, the main XRD peak of this phase, detected at 22° in the XRD patterns, always displayed a low intensity.[13] To ascertain the locations of the Li ions, the intensity of the central line of the ^7Li MAS NMR spectra, normalized to the amount of sample, is plotted vs x in Figure 7c. We again observe that, below $x = 0.2$, lithium is mainly placed into the NASICON framework, as deduced from the good agreement between the experimental (circles) and predicted (solid line) data. However, above $x = 0.2$, the experimental data are lower than predicted, indicating again that a part of the Li is placed in phases other than that of the NASICON compounds.

At this point, it is interesting to analyze the conductivity of the samples with $x \leq 0.2$. For the grain interior conductivity, plots of the activation energy (E) and preexponential factor (σ_0) vs x are given in Figure 8a. We observe that σ_0 decreases as x increases, despite the fact that the Li content increases as $1 + x$. The decrease in σ_0 cannot explain the increase observed in conductivity along the series. The increase in conductivity must be associated with the decrease observed in E as x increases. However, the decrease found in E differs from the results reported previously in the same series, where

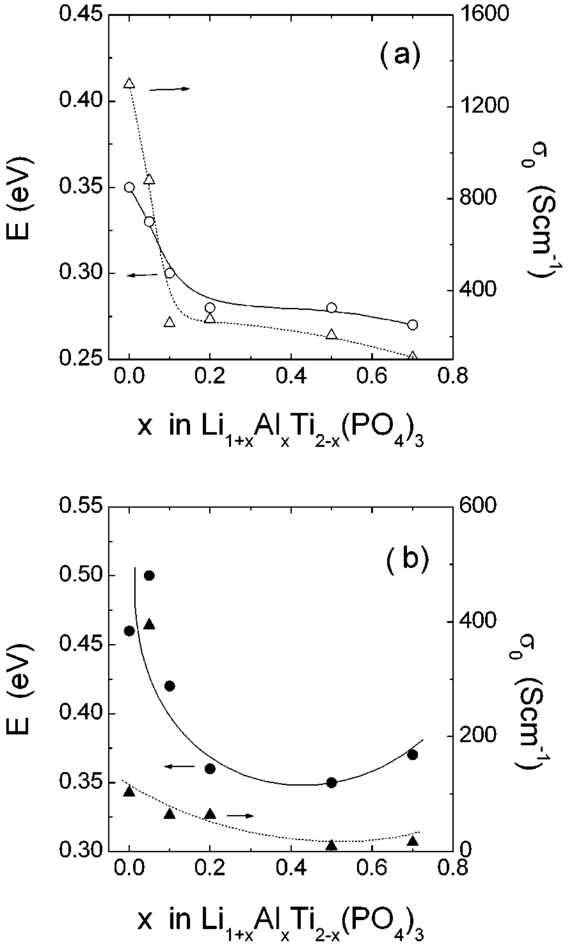

Figure 8. Pre-exponential factor (σ_0) and activation energy (E) as functions of the Al content: (a) grain interior conductivity, (b) overall conductivity. The solid and dashed lines are guides to the eye.

E does not vary with x.[13,27] The observed decrease in E occurs in parallel with a decrease in the size of the hexagonal unit cell. This trend is opposite to that found in stoichiometric $LiM_2(PO_4)_3$ compounds, where a decrease in E was accompanied by an increase in the hexagonal unit cell parameters.[6]

In the $LiTi_2(PO_4)_3$ sample, the Li^+ ions preferentially occupy the M1 sites.[11] In agreement with this fact, the quadrupole constants deduced from the ^7Li NMR spectra, $C_Q = 42$ kHz and $\eta = 0$, are characteristic of undistorted sites with axial symmetry.[28] In $Li_{1+x}Ti_{2-x}Al_x(PO_4)_3$ samples, the higher lithium content makes Li ions occupy, in addition to the M_1 sites, other more distorted sites between the M_1 sites in the conducting paths.[5] This fact shortens the Li–Li distance, thus destabilizing the occupancy of the M_1 sites and presumably enhancing the Li mobility. In agreement with these predictions, a high mobility of lithium was deduced in all samples from an analysis of the line width of ^7Li NMR spectra recorded under static conditions. This finding is similar to that reported previously by Forsyth et al.[25] According to this fact, an exchange process between the two structural sites must be

---

(27) Aono, H.; Sugimoto, E.; Sadaoka, Y.; Imanaka, N.; Adachi, G. *Chem. Lett.* **1990**, 1825–1828.

(28) París, M. A.; Martinez-Juárez, A.; Rojo, J. M.; Sanz, J. *J. Phys. Condens. Matter* **1996**, *8*, 5355–5366.

favored, which would explain the slight increase observed in the averaged quadrupole constant C_Q along the series[5] (Table 1).

For the overall conductivity, we observe that σ_0 is almost constant but E decreases gradually with x for $x \leq 0.2$ (Figure 8b). The decrease of E accounts for the increase observed in conductivity. Although Al and Li are preferentially incorporated into the NASICON framework in the compositional range analyzed, appreciable amounts of the two metals seem to be segregated in a phase that is not detected by the XRD technique. The detection of new broad lines at 40 and −30 ppm in the ^{27}Al and ^{31}P MAS NMR spectra, respectively, suggests that an amorphous aluminum phosphate is formed.[29] In this phase, Li^+ ions should be incorporated, as deduced from the analysis of the intensity of the central line of ^{7}Li MAS NMR spectra vs aluminum content (Figure 7c). The presence of lithium in the amorphous phase would spread the intensity of the NMR signal over a broad region, reducing the visibility of Li at the center of the spectrum. The formation of a conducting phase at the grain boundaries of the major NASICON phase increases the overall conductivity of the pellets and decreases their porosity.[13,25]

Samples with $x > 0.2$. In these samples, the grain interior conductivity does not change appreciably, in agreement with the fact that E and σ_0 remain almost constant (Figure 8a). This observation parallels to the slight variation of the unit cell parameters and indicates that, above $x = 0.2$, the amounts of Al and Li incorporated into the NASICON framework are lower than expected. This conclusion is supported by the NMR results, which show lower experimental Al_O and Li values than expected from the nominal NASICON compositions (Figure 7). Therefore, some Al and Li must be segregated in other phases. The lack of new reflections in the XRD patterns and the appearance of broad peaks in the ^{27}Al and ^{31}P NMR signals suggest that the segregated Al and Li are located in an amorphous phosphate probably surrounding the NASICON particles.

The nature of the amorphous segregated phase changes drastically along the series. For $x > 0.3$, the Al_T line increases considerably and shifts toward lower values, and a new Al_O line is detected in the ^{27}Al MAS NMR spectra (Figure 2). Moreover, the intensity of the new NMR line detected at −29 ppm in the ^{31}P MAS NMR spectra increases with the Al content indicating that the amount of amorphous aluminum phosphate increases significantly. On the other hand, the XRD patterns show the presence of the crystalline $Li_4P_2O_7$ phase (Figure 1a). This is confirmed by the detection of new components at ~0 ppm in the ^{7}Li MAS NMR spectra and at −19 ppm in the ^{31}P MAS NMR spectra of the $x = 0.5$ and 0.7 samples. The appearance of $Li_4P_2O_7$ is accompanied by the newly found electrical response (Figure 6).

The overall conductivity of the pellets decreases as x increases in the compositional range $0.3 < x < 0.7$. This decrease is associated with the slight decrease observed in σ_0 and the slight increase observed in E (Figure 8b). Because the ionic conductivity of $Li_4P_2O_7$ is higher than the overall (grain boundary) conductivity, the formation of this crystalline phase should not produce any decrease in the overall conductivity of the pellet. From this fact, we can establish that the decrease observed in conductivity must be ascribed to a modification of the amorphous phase. At first sight, the formation of $Li_4P_2O_7$ should extract Li from the amorphous phase, thus decreasing the amount of charge carriers and hence decreasing σ_0. However, the increase observed in the activation energy E indicates that the local structure of the amorphous phase is also changed. The formation of an insulating phase similar to $AlPO_4$ among the NASICON particles must block the conducting paths previously established for Li^+ ions and must lead to a decrease of the overall conductivity. The observation of a maximum in the overall conductivity of the analyzed series agrees with that reported for other ion-conducting composites.[30,31]

V. Conclusions

The complementary use of XRD and NMR techniques has permitted the analysis of nominal $Li_{1+x}Ti_{2-x}Al_x(PO_4)_3$ samples and the detection of secondary phases formed during their preparation. For samples with $x \leq 0.2$, substitution of Ti^{4+} by Al^{3+} in the Ti-based NASICONs $Li_{1+x}Ti_{2-x}Al_x(PO_4)_3$ reduces the unit cell dimensions but increases the amount of Li^+ ions and increases the grain interior conductivity. For $x > 0.2$, the grain interior conductivity does not change appreciably.

In the analyzed samples, the overall conductivity is mainly affected by the composition of the segregated amorphous phase. Below $x = 0.2$, the presence of the amorphous lithium-conducting phase between NASICON particles increases the overall conductivity of samples. For $x > 0.2$, the formation of $Li_4P_2O_7$ reduces the Li content and modifies the structure of the amorphous phase; both facts account for the decrease observed in the overall conductivity.

Acknowledgment. Financial support provided by CICYT, Projects MAT98-1053-CO4-03 and MAT98-0904, is gratefully acknowledged. K.A. and S.M. thank the AECI and the Spanish Ministry of Education and Culture, for their respective fellowships.

CM010528I

---

(29) Phillips, B. R.; Kirkpatrik, R. J.; Thompson, J. G. *Nuclear Magnetic Shieldings and Molecular Structure*; Tossel, J. A., Ed.; Kluwer Academic Publishers: Dordrecht, The Netherlands, 1993; p 212.

(30) Uvarov, N.; Hairanddinov, E. F.; Skobelev, I. V. *Solid State Ionics* **1996**, *86−88*, 577−580.

(31) Takada, M.; Tansho, I.; Yanase, I.; Inada, T.; Kajiyama, A.; Kouguchi, M.; Kondo, S.; Watanabe, M. *Solid State Ionics* **2001**, *139*, 241−247.